The Astrophysical Journal, 804:107 (11pp), 2015 May 10 doi:10.1088/0004-637X/804/2/107
© 2015. The American Astronomical Society. All rights reserved.

THE MULTI-LAYER VARIABLE ABSORBERS IN NGC 1365 REVEALED BY *XMM-NEWTON* AND *NuSTAR*

E. Rivers[1], G. Risaliti[2,3], D. J. Walton[4,1], F. Harrison[1], P. Arévalo[5], F. E. Baur[6,7], S. E. Boggs[8], L. W. Brenneman[3], M. Brightman[1], F. E. Christensen[9], W. W. Craig[8], F. Fürst[1], C. J. Hailey[10], R. C. Hickox[11], A. Marinucci[12], J. Reeves[13], D. Stern[4], and W. W. Zhang[14]

[1] Cahill Center for Astronomy and Astrophysics, California Institute of Technology, Pasadena, CA 91125, USA
[2] INAF—Osservatorio Astrofisico di Arcetri, Largo Enrico Fermi 5, I-50125 Firenze, Italy
[3] Harvard-Smithsonian Center for Astrophysics, 60 Garden Street, Cambridge, MA 02138, USA
[4] Jet Propulsion Laboratory, California Institute of Technology, Pasadena, CA 91109, USA
[5] Instituto de Física y Astronomía, Facultad de Ciencias, Universidad de Valparaíso, Gran Bretana N 1111, Playa Ancha, Valparaíso, Chile
[6] Pontificia Universidad Católica de Chile, Instituto de Astrofísica, Casilla 306, Santiago 22, Chile
[7] Space Science Institute, 4750 Walnut Street, Suite 205, Boulder, Colorado 80301, USA
[8] Space Sciences Laboratory, University of California, Berkeley, CA 94720, USA
[9] DTU Space, National Space Institute, Technical University of Denmark, Elektrovej 327, DK-2800 Lyngby, Denmark
[10] Columbia Astrophysics Laboratory, Columbia University, New York, NY 10027, USA
[11] Department of Physics and Astronomy, Dartmouth College, 6127 Wilder Laboratory, Hanover, NH 03755, USA
[12] Dipartimento di Matematica e Fisica, Universita degli Studi Roma Tre, via della Vasca Navale 84, I-00146 Roma, Italy
[13] Astrophysics Group, School of Physical and Geographical Sciences, Keele University, Keele, Staffordshire, ST5 5BG, UK
[14] NASA Goddard Space Flight Center, Greenbelt, MD 20771, USA
Received 2014 November 7; accepted 2015 March 6; published 2015 May 7

ABSTRACT

Between 2012 July and 2013 February, *NuSTAR* and *XMM-Newton* performed four long-look joint observations of the type 1.8 Seyfert, NGC 1365. We have analyzed the variable absorption seen in these observations in order to characterize the geometry of the absorbing material. Two of the observations caught NGC 1365 in an unusually low absorption state, revealing complexity in the multi-layer absorber that had previously been hidden. We find the need for three distinct zones of neutral absorption in addition to the two zones of ionized absorption and the Compton-thick torus previously seen in this source. The most prominent absorber is likely associated with broad-line region clouds with column densities of around $\sim 10^{23}$ cm^{-2} and a highly clumpy nature as evidenced by an occultation event in 2013 February. We also find evidence of a patchy absorber with a variable column around $\sim 10^{22}$ cm^{-2} and a line-of-sight covering fraction of 0.3–0.9, which responds directly to the intrinsic source flux, possibly due to a wind geometry. A full-covering, constant absorber with a low column density of $\sim 1 \times 10^{22}$ cm^{-2} is also present, though the location of this low density haze is unknown.

Key words: galaxies: active – galaxies: individual (NGC 1365) – X-rays: galaxies

1. INTRODUCTION

NGC 1365 is a Seyfert 1.8 active galactic nucleus (AGN) that exhibits a highly complex and variable X-ray spectrum. In addition to the power-law continuum which is thought to arise in a hot corona very close to the central supermassive black hole, the X-ray spectrum shows a strong Compton reflection hump peaking at 20–30 keV (see e.g., George & Fabian 1991; Walton et al. 2010) and a prominent Fe K emission complex (Risaliti et al. 2009, 2013), both of which are signatures of reflection off Compton-thick material. Extended X-ray emission from plasma and starburst activity below ~2 keV have been characterized by *Chandra* (Wang et al. 2009) and *XMM-Newton* (Guainazzi et al. 2009). Absorption lines from ionized Fe species in the ~7–8 keV range are thought to arise in a highly ionized ($\xi \sim 10^3$–10^4 erg cm s^{-1}) high-velocity outflow ($v \sim 1000$–5000 km s^{-1}) that varies on timescales of days to months (Risaliti et al. 2005; Brenneman et al. 2013). The mass of the central black hole has been estimated from the $H\beta$ width to be $M_{\rm BH} \sim 2 \times 10^6\ M_\odot$ (Risaliti et al. 2009 and references therein), implying an Eddington ratio of 0.02 to 0.12 $L/L_{\rm Edd}$.

Due to the complexity of this source, broad energy coverage is necessary in order to accurately characterize the X-ray spectrum. Four simultaneous *XMM-Newton* and *NuSTAR* observations were taken in 2012 and 2013 with the primary aim of studying the broad Fe Kα line and prominent reflection hump in this source likely associated with relativistic reflection from the inner regions of the accretion disk (Risaliti et al. 2013). Measurements of the black hole spin from modeling the relativistic reflection indicate a rapidly rotating black hole with a dimensionless spin parameter $a \gtrsim 0.95$ (Risaliti et al. 2013; Walton et al. 2014), consistent with previous measurements (Brenneman et al. 2013), though with higher signal-to-noise broadband spectra. Other work on this dataset by Kara et al. (2015) showed that the Fe Kα line and Compton reflection hump lag the continuum on the same timescales and Walton et al. (2014) found a correlation between the strengths of the Fe Kα line and the Compton hump. This connection is important in establishing that the broadness in the line is indeed associated with reflection from the accretion disk, rather than being due to absorption or some other spectral variance.

These joint *XMM-Newton*/*NuSTAR* observations revealed strong variability in the flux as well as in the spectral shape. Walton et al. (2014) found that the majority of the spectral variability was due to variable line-of-sight absorption, a result that was subsequently confirmed by principal component analysis (Parker et al. 2014). Two of the observations caught the source in an unusually low absorption state, and the third of these observations actually showed an almost complete uncovering of the source. Braito et al. (2014) have analyzed the *XMM-Newton* RGS spectrum from this observation and

Table 1
Observation Details

Observation	1	2	3	4
NuSTAR ObsID	60002046002/3	60002046005	60002046007	60002046009
FPMA Net Exposure Time (ks)	77	66	74	70
FPMB Net Exposure Time (ks)	77	66	74	70
XMM-Newton ObsID	0692840201	0692840301	0692840401	0692840501
MOS Net Exposure Time (ks)	134	122	105	122
PN Net Exposure Time (ks)	118	108	93	116

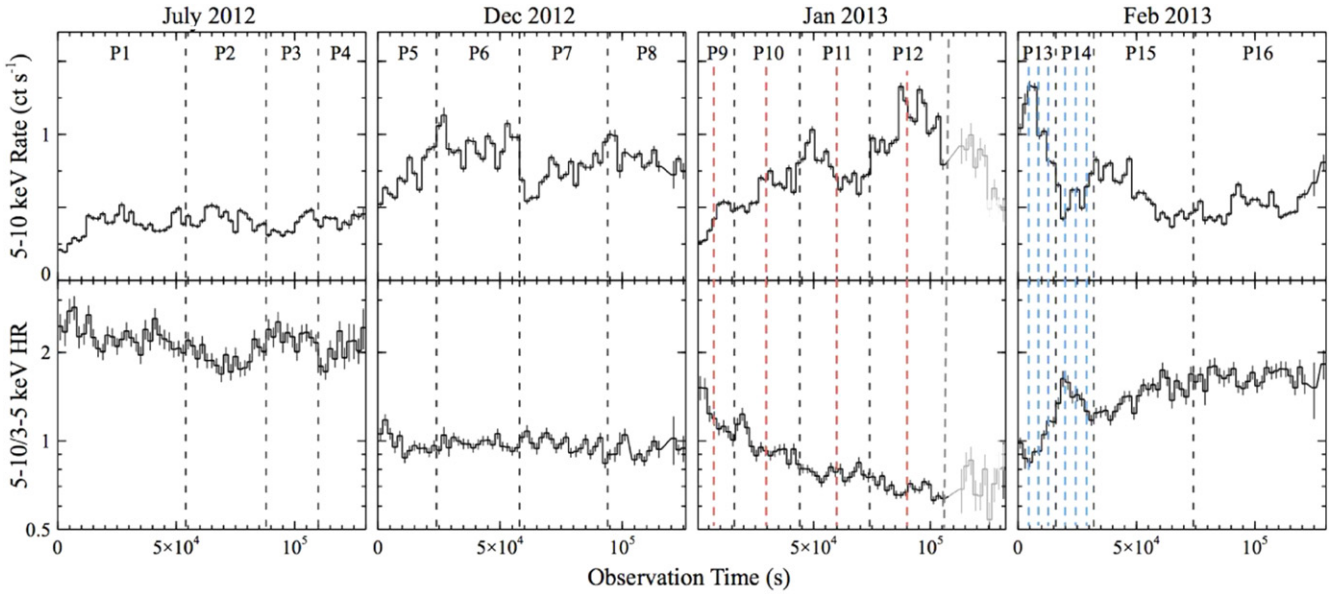

Figure 1. Light curves for all four observations showing 5–10 keV observed flux (top) and 5–10/3–5 keV hardness ratio (bottom). Dashed lines indicate time-resolved analysis intervals: P1–16 (black), the eight subintervals of observation 3 (red), and the eight subintervals of observation 4 (blue). Note that the gray data points at the end of observation 3 were excluded from analysis. A background flare occurred during this time creating large uncertainties, particularly for time-resolved analysis.

found evidence for a mildly ionized wind absorber in addition to the previously known highly ionized wind absorber that is only evident when the source is uncovered and at a high luminosity level. This paper aims to analyze the variable absorption seen in all four joint *XMM-Newton*/*NuSTAR* observations in order to further characterize the geometry of the absorbing material in this source.

Variable absorption is not uncommon in Seyfert galaxies on a wide range of timescales, from hours (MCG 6-30-15: Marinucci et al. 2014) to months (NGC 3227—Lamer et al. 2003; Cen A—Rivers et al. 2011), to years (NGC 3516—Turner et al. 2008; NGC 2110—Rivers et al. 2014). Changes over a timescale of years may be due to a global change in the amount of material surrounding the supermassive black hole, while changes on shorter timescales (hours to months) are likely a result of inhomogeneous material. Lamer et al. (2003) characterized an occultation event in NGC 3227 that showed a smooth rise and fall in the column density due to the ingress into and egress out of the line-of-sight of a clump of material which was thought to be part of the broad-line region (BLR). A similar event lasting around 60 days was seen in Cen A (Rivers et al. 2011) but was found to originate in the infrared torus, consistent with the clumpy torus models set forth by Nenkova et al. (2008).

In the past, the absorption column in the line-of-sight to NGC 1365 has been seen to exhibit rapid variability on timescales of hours to days (Risaliti et al. 2009). This is thought to be due to BLR clouds passing through the line-of-sight (Maiolino et al. 2010). On longer timescales, the absorbing column has been seen to vary widely with a range of column densities spanning $N_{\rm H} \sim 10^{22}-10^{24}$ cm^{-2} (Connolly et al. 2014). Connolly et al. (2014) also noticed an anti-correlation between the column density and the intrinsic luminosity, which they suggest could be explained by winds with variable launch radii.

This paper is structured as follows: Section 2 contains details of the observations and data reduction, Section 3 describes the spectral analysis with limited interpretation, and Section 4 discusses our results and the conclusions we can draw from them.

2. OBSERVATIONS AND DATA REDUCTION

Data were taken 2012 July, 2012 December, 2013 January, and 2013 February with *XMM-Newton* and *NuSTAR* simultaneously. Table 1 shows a log of the observations. All extractions were done using HEASOFT v.6.13.

In order to explore the changing spectral parameters, we have performed time-resolved spectral analysis. In addition to

characterizing the four individual observations, each has been further subdivided into a total of 16 intervals (four per observation) based on flux and hardness level as seen in Figure 1, identical to those of Walton et al. (2014). Additionally, we have performed an analysis on very short timescales where rapid changes in the absorption column are observed: eight half intervals for observation 3 and eight 4 ks intervals for the first 32 ks (two intervals) of observation 4.

2.1. XMM-Newton Reduction

We reduced the *XMM-Newton* data for all four observations using the Science Analysis System (v13.0.0) following the procedure detailed in the online guide and Walton et al. (2014). We processed the data using EPPROC and EMPROC for the EPIC-pn (Strüder et al. 2001) and EPIC-MOS (Turner et al. 2001) data, respectively. Spectra and light curves were extracted from circular source and background regions with 40″ and 50″ radius for the pn and MOS, respectively. Response and ancillary response matrices were generated using the FTOOLs RMFGEN and ARFGEN.

During the last portion of observation 3 the source reached a peak in the flux level sufficient for pile-up to be a concern. We found some evidence for pileup in the MOS below 10 keV, and therefore excluded the central 8″ for the pn and 10″ for the MOS for observation 3 and interval P12 (the last interval of observation 3). Note that we did not include data from observation 3 past 110 ks where a background flare occurred, possibly contaminating the data (see Figure 1).

2.2. NuSTAR Reduction

We reduced data from both *NuSTAR* modules, FPMA and FPMB (Harrison et al. 2013), using the standard pipeline in the *NuSTAR* Data Analysis Software v1.1.1. Instrumental responses were taken from the *NuSTAR* CALDB v20130315. The unfiltered event files were cleaned with the standard depth correction, which significantly reduces the internal background at high energies, and SAA passages were excluded from our analysis. For both modules we extracted spectra and light curves from a 100″ circular source region and a 100″ background region on the same chip as the source. We grouped the *NuSTAR* spectra with a minimum of 25 counts per bin.

3. SPECTRAL ANALYSIS

All spectral fitting was done in XSPEC v.12.8.0 (Arnaud 1996) using the solar abundances of Anders & Grevesse (1989) with cross sections from Verner et al. (1996). Uncertainties are listed at the 90% confidence level ($\Delta\chi^2 = 2.71$ for one interesting parameter). We included a constant offset for each instrument as a free parameter to account for known cross calibration uncertainties and included a Galactic absorption column of 1.34×10^{20} cm^{-2} in all models (Kalberla et al. 2005).

3.1. Initial Modeling

Initially we fit each of the four observations separately in the 3–70 keV range with an absorbed power-law. This fit was universally poor (χ^2/degrees of freedom (dof) = 2832/1047, 6926/1145, 4551/1137, and 3968/1113 for observations 1, 2, 3, and 4, respectively) and showed strong residuals in the Fe K bandpass (~5–9 keV) as well as broad residuals in the 20–30 keV range (see Figure 1 of Risaliti et al. 2013; Walton et al. 2014 for which the continuum and reflection modeling of these data has been done in great detail). In order to model the apparent neutral Fe emission lines we added a neutral reflection component. We used the XILLVER XSPEC model, which includes Fe K emission lines and a Compton reflection hump from a disk geometry (García & Kallman 2010). There was significant improvement in the fit statistic for each observation (χ^2/dof = 2106/1044, 5727/1142, 3630/1134, and 3059/1110). Note that this model choice was not a significant improvement over a phenomenological modeling using multiple Gaussian components and a neutral Compton hump such as from PEXRAV, but we prefer a self-consistent physical model whenever possible.

Strong negative residuals in the Fe K band remained, necessitating the addition of four absorption lines from highly ionized species of Fe in a high velocity outflow (Risaliti et al. 2005; Brenneman et al. 2013). We tied the velocities and line widths of the four lines, assuming intrinsic line energies of 6.70, 6.97, 7.88, and 8.27 keV. This greatly improved the fit statistics (χ^2/dof = 1341/1039, 2325/1137, 2197/1129, and 1784.1/1105), though broad residuals still remained near the Fe Kα line and above 10 keV. Though there are several models available which might be used at this juncture, we have elected to use RELCONV ×XILLVER to model relativistic reflection from the inner parts of an ionized accretion disk. Inclination angle, ionization state, Fe abundance, black hole spin, and normalization were left as free parameters in our initial fitting. This model provided a good fit to the data in all four observations (χ^2/dof = 1087/1035, 1445/1133, 1283/1125, and 1300/1101, for the four observations, respectively). Parameter values, detailed justification of the model, and physical interpretations for this analysis can be found in Walton et al. (2014).

Those parameters that we expect to remain constant over the timescale of our observations were frozen at their average values: black hole spin (0.98), disk inclination (63°), Fe abundance (4.7). Note that modeling the distant reflection with a torus model can lead to a much lower measurement of the Fe abundance for the distant reflector; however, this does not change our primary results so for simplicity we adhere to the model presented in Walton et al. (2014), tying the Fe abundance between the two reflectors. We also froze the following parameters that showed no evidence for variability over the four observations: ionization of the inner disk ($\log\xi = 1.8$), and disk emissivity index (6.75). Note that we do not see evidence for a high energy cutoff in this source and it was therefore not included in our final model.

3.2. Modeling the Spectrum Below 1 keV

In order to fully characterize the partial-covering absorption in this source, we must extend our spectral analysis down to lower energies. It was immediately evident that observations 2 and 3, and possibly observation 4, were partially unobscured in the 1–3 keV range. We therefore replaced the full-covering absorber in our model with a partial-covering absorber, though for observation 1 the covering fraction remained pegged at 1. Additionally, we chose to analyze the spectrum down to 0.4 keV in order to model the soft emission from diffuse plasma in the region so that we could be confident that our measurements of the absorption were not influenced by this component.

The extended plasma was previously studied in detail by Wang et al. (2009) using *Chandra* gratings data and by

Guainazzi et al. (2009) using *XMM-Newton* RGS data. These analyses determined that the plasma was likely a combination of thermal and photoionized plasma. When the AGN is in an absorbed state the extended plasma dominates the soft X-ray flux and it is expected to remain essentially constant due to its spatial extent. For our modeling we used a phenomenological double APEC component (i.e., two-temperature collisionally ionized gas) with temperatures of 0.3 and ~0.8 keV, and five additional Gaussian components to model emission line complexes from photoionized gas at 0.50, 0.85, 1.03, 1.24, and 2.74 keV, similar to Brenneman et al. (2013). These components are shown in red in Figure 2. We determined the normalizations of these components using data from observation 1 only because it is the only observation that is fully covered and therefore allowed for the best determination of the plasma parameters. Since we do not expect the extended plasma to undergo any changes over the months between our observations we froze these parameters to those measured in observation 1. We included an additional soft power-law component in the modeling to account for differences in flux level below 2 keV for the four observations. The photon index was tied to that of the primary continuum power-law and in all fits was found to have a normalization around ~2% that of the primary power-law, as expected for a scattered continuum component (e.g., Turner et al. 1997; Guainazzi et al. 2005; Eguchi et al. 2009). Compared to the flux of the combined plasma components, $F_{0.5-2} = 3.6 \times 10^{-13}$ erg cm^{-2} s^{-1}, the scattered power-law 0.5–2 keV flux values were 2.7×10^{-13} erg cm^{-2} s^{-1}, 4.4×10^{-13} erg cm^{-2} s^{-1}, 7.8×10^{-13} erg cm^{-2} s^{-1}, and 3.5×10^{-13} erg cm^{-2} s^{-1}for the four observations, respectively.

We applied this model to the other three observations and discovered the need for an additional layer of full-covering absorption, with an improvement in fit of $\Delta\chi^2$/dof = 6000/1 for observation 2, $\Delta\chi^2$/dof = 1500/1 for observation 3, and $\Delta\chi^2$/dof = 1050/1 for observation 4, with a column density of $N_{\rm H} \sim 1 \times 10^{22}$ cm^{-2} for all three observations. We will refer to this absorbing layer as the "full-covering low column" absorber for the remainder of the paper. Given the consistency of this component over the last three observations it seems reasonable to assume that it is also present in observation 1, but it is completely degenerate with the higher column density absorber which is fully covering during that observation. We have included the component in our modeling of observation 1 with a fixed column density of 1.0×10^{22} cm^{-2}in the hopes that this gives us a more accurate measurement of the column density of the partial-covering absorber layer during that observation.

We also found unexpected variability below 1 keV which was not fit by the changing absorption or the scattered power-law. The unidentified excess appeared in the less absorbed observations, strongest in observations 2 and 3, while completely absent in observation 1. None of the usual components that might account for this increase in flux below 1 keV were able to fit the data (i.e., a blackbody or power-law soft excess, changes in the fully covering absorber, or reflection from ionized material). We therefore fit the excess with an additional phenomenological Gaussian at 0.68 keV with a width of $\sigma \sim$ 200 eV. Including this component resulted in an improvement in the fit of $\Delta\chi^2$/dof = 200/3 for observation 3 and $\Delta\chi^2$/dof = 30/3 for observation 2, with a null hypothesis probability of 4×10^{-4}. It was not significant to include the component in observations 1 or 4, both of which result in a normalization of the component consistent with 0. We investigate the source of this feature in Section 3.6. Residuals to models excluding the full-covering low column absorber and the phenomenological Gaussian are shown for each observation in Figure 2, panels (c) and (d), respectively.

3.3. The Final Model and Time Resolved Fitting

Our final model consisted of two collisional plasma components plus five Gaussian emission lines to model the extended plasma, a scattered power-law, the phenomenological Gaussian at 0.68 keV, a full-covering neutral absorber ($N_{\rm H} \sim 1 \times 10^{22}$ cm^{-2}), a partial covering neutral absorber, four absorption lines from highly ionized species of Fe in a high velocity outflow, a continuum power-law, relativistic disk reflection, and cold distant reflection. The final form of the model in XSPEC is: APEC[×2] + ZGAUSS[×5] + SCATTERED POWERLAW + GAUSS + ZPHABS × ZPCFABS × GAUABS[×4] × (POWERLAW + RELCONV × XILLVER) + XILLVER.

For consistency checks, we fit all four observations simultaneously, exploring which parameters were consistent across the observations. We find that the full-covering absorber was very steady over all three observations where it was measurable. In observation 1 this layer is completely degenerate with the high column density layer of absorption. We therefore included this layer in all fits to observation 1 with a column density frozen at 1.0×10^{22} cm^{-2}. Figure 2 shows each of the four observations with final best-fit model components in panel (a) and residuals to the best-fit model in panel (e). Parameters are listed in Table 2.

We then fit the 16 intervals independently in the 0.3–70 keV range using our final model. In order to reduce degeneracy we froze the column density of the full-covering constant absorber to the time-averaged value for each observation and to 1.0×10^{22} cm^{-2} for all intervals of observation 1. Best-fit parameters for all 16 intervals are listed in Table 2 and the evolution of the parameters with the most interesting variability ($N_{\rm H}$, f, Γ, and intrinsic flux) is shown in Figure 3. Values for the Fe K ionized wind absorption were also left free, but did not vary significantly over the observations (i.e., they varied by less than the measured error bars).

3.4. The Uncovering of the Source in Observation 3

In observation 3 we saw a dramatic drop in the absorption by the partial-covering absorber. The line-of-sight covering fraction (f) fell from 0.9 to 0.3 over the course of the observation, almost completely uncovering the source. The column density also dropped significantly (nearly a factor of 2) to 5×10^{22} cm^{-2}. Figure 3 shows the rapid decrease in both parameters with a corresponding increase in the unabsorbed power-law flux. In order to get a clearer picture of the evolution of these parameters we performed additional time-resolved analysis on observation 3, breaking each interval in half and fitting the 8 subintervals. We used the final model as described in Section 3.3 with the full-covering absorber column density held fixed at the time-averaged value of 1.1×10^{22} cm^{-2}.

Figure 4 shows the evolution of the column density, covering fraction, photon index, and intrinsic power-law flux for observation 3. The rapid decrease in both $N_{\rm H}$ and f could plausibly be due to parameter degeneracy; however, the error

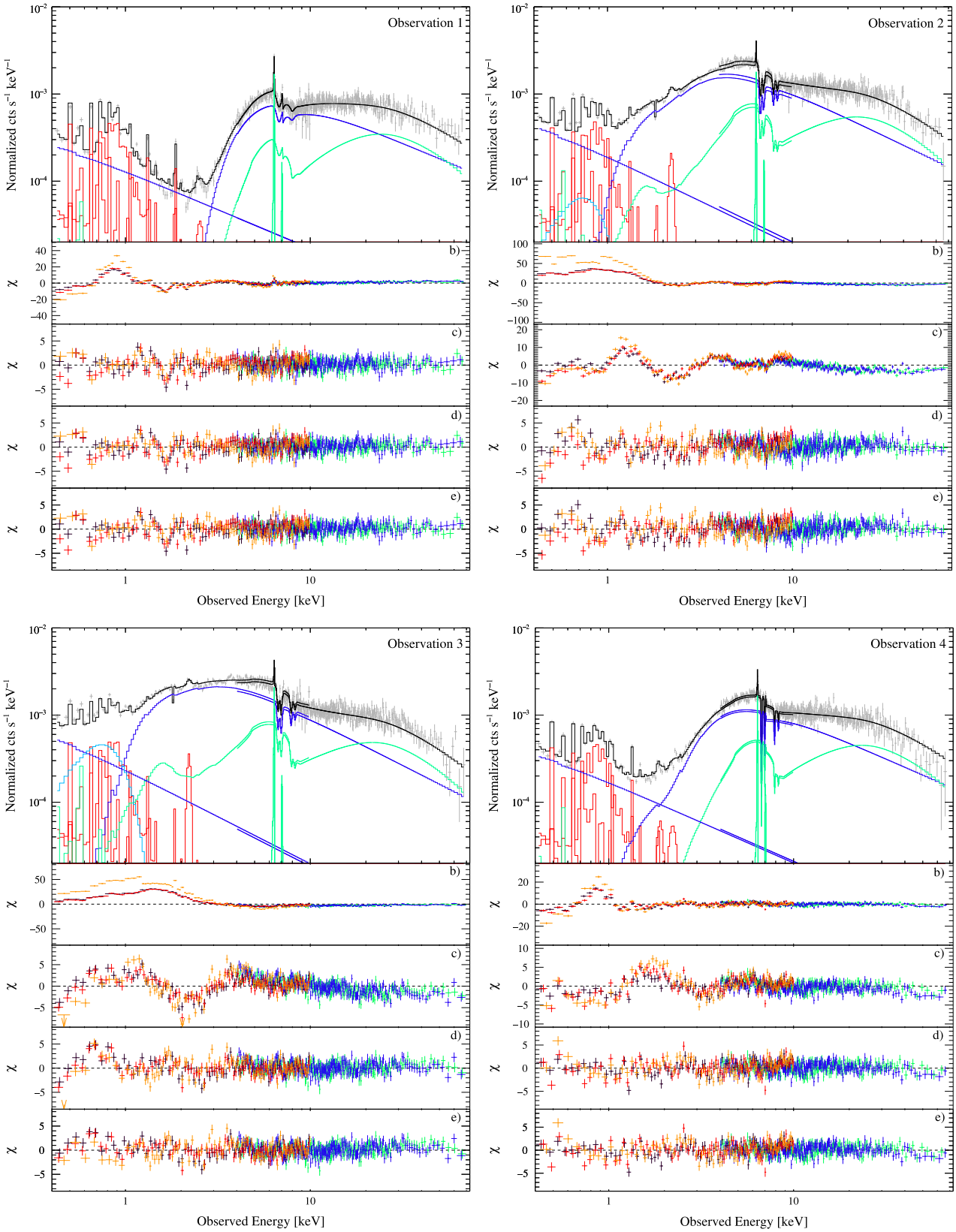

Figure 2. Panel (a) shows the 0.4–70 keV unfolded spectra of all four observations (PN + FPMA in gray) with full model (black), absorbed and scattered power-laws (blue), extended plasma components (red), relativistic and cold/distant reflection (green), and the phenomenological Gaussian component (light blue). Residuals are shown in panels (b)–(e) with red and orange data points corresponding to *XMM-Newton* MOS1 and MOS2, respectively, purple data points corresponding to PN data, and blue and green data points corresponding to *NuSTAR* FPMA and FPMB, respectively. Panel (b) shows the best fit to the initial model as described in Section 3.1 before including the extended plasma, scattered power-law, or additional absorption complexity. Panel (c) shows the best fit to a model including the extended plasma but with only one neutral absorber component (partial-covering). Panel (d) shows the best fit to a model without the phenomenological Gaussian at 0.68 keV. Panel (e) shows the best fit to our final model for each observation as described in the text with parameters given in Table 2.

bars seem too small for this to be the case. A contour plot of N_H versus f for the eight subintervals shown in Figure 5 verifies that little to no parameter degeneracy is apparent between N_H and f. While there is an expected degeneracy between the column density and flux of the source shown in Figure 6, it is generally small compared to the changes in the parameters and is in the opposite sense to the observed evolution.

The decreasing column density and covering fraction both seem to have an inverse relationship with the increasing intrinsic flux. The photon index is relatively stable over the same period. This is unusual behavior for absorption variability caused by clumps moving into and out of the line-of-sight. Column density and covering fraction do not typically vary in lock step with one another and we would not expect either parameter to correlate with intrinsic flux. This may be indicative of an evolution in the absorbing material with luminosity, such as in the wind absorber scenario proposed by Connolly et al. (2014; discussed in Section 4.1). We will refer to this layer of absorption (seen primarily in observation 3) as the "patchy partial-covering" absorber to distinguish it from the sometimes partial-covering "high column density" absorber, which dominates in observations 1 and 4.

3.5. Occultation Event in Observation 4

Observation 4 shows a rapid increase in column density during the first 32 ks (intervals P13 and P14), with little to no change in the covering fraction. We broke the first 32 ks down into eight 4 ks subintervals and fit just the PN+FPMA data in the 1–40 keV range for computational brevity, using the final model as described in Section 3.3. Parameters for the full-covering absorber, scattered power-law, highly ionized wind absorber, and reflection were also held constant. We find an evolution of the continuum and absorption parameters shown in Figure 7. The column density peaked around 20–24 ks, with a seemingly symmetrical profile strongly indicative of a clump of material passing through the line-of-sight. Though degeneracy between the column density and intrinsic flux is again present in these fits, the lack of change in the covering fraction makes this behavior very different from that seen in observation 3. Again, the level of degeneracy is less than the observed changes (see Figure 8).

If this is indeed an occultation event then it is consistent in duration with events seen previously in this source and thought to be due to BLR clouds passing through the line-of-sight (Maiolino et al. 2010). Using their estimate for R_{BLR} of $\sim 10^{16}$ cm, and assuming a black hole mass of $2 \times 10^6\ M_\odot$ we estimate the velocity of the cloud in a circular orbit to be $\sim 1600\ \mathrm{km\ s^{-1}}$. Following the analysis of Rivers et al. (2011) for a smooth, symmetrical occultation event assuming a circular orbit around the black hole, we fit the absorption profile with a solid sphere, a beta profile ($\rho \propto r^{\beta}$) and a sphere of linear density profile ($\rho \propto r^{-1}$), shown in Figure 9. We find a cloud size of $\sim 4 \times 10^{12}$ cm ($\sim 10\ R_g$) with a central density of $\sim 3 \times 10^{10}\ \mathrm{cm^{-3}}$ for the linearly decreasing density sphere. These numbers are consistent with the physical properties inferred by Maiolino et al. (2010) for the cloud cores, although we do not see evidence of the same cometary structure inferred in that work (N_H rises again after the first 32 ks of observation 4 and the covering factor is relatively stable over the course of the event).

3.6. The Additional Soft Component

From Table 2 we see that the phenomenological Gaussian component at 0.68 keV peaks strongly in observation 3. The strength of this feature seems to be anti-correlated with the covering fraction, not showing up at all in observation 1, which is fully covered, and only very weakly in observation 4 where the covering fraction is 0.97–1.0. This component is therefore clearly not associated with the extended plasma and likely arises within the radius of the variable high column density partial-covering absorber.

Braito et al. (2014) have analyzed the RGS spectrum of observation 3 and found evidence for an increasing ionization in their low column absorber over the course of the observation. What we are seeing in the MOS/PN may be due to further leakage of the power-law below 1 keV due to increasing ionization of the low column full-covering absorber as the source increases in luminosity. The material would have to be quite close to the central source since it is directly correlated with the observed increase in intrinsic power-law flux. With time-resolved fitting on timescales of around 20 ks this would mean the material is at a distance of $\lesssim 10^{16}$ cm, which is roughly the radius of the BLR and is consistent with being inside the radius of the high column density partial-covering absorber.

Another possibility is the uncovering of actual emission lines such as from O VIII Lyα at 0.654 keV. This could be from highly ionized material that is very close to the central source and only visible when the full-covering low column absorber becomes ionized enough to be semi-transparent at energies below 1 keV. Braito et al. (2014) also noticed that some broader soft X-ray lines started to emerge during the last part of observation 3, for instance from Mg XI and Mg XII, which were much broader than the usual distant narrow line emission, and which seemed to have P Cygni like profiles. These lines could be associated with a disk wind very close to the central source. It is worth noting that a visual inspection of the RGS residuals in Figure 4 of Braito et al. (2014) reveals systematically high residuals around 0.65–0.7 keV.

4. DISCUSSION AND CONCLUSIONS

From our spectroscopic analysis of NGC 1365 we begin to understand the full complexity of the multi-layer absorption. It has long been known that the central nucleus is surrounded by patchy material that provides distant reflection and variable absorption of the X-ray corona, both on short timescales (hours) that are likely associated with eclipsing BLR clouds, and on longer timescales (days to months) that are likely associated with slowly moving material in the torus.

A full-covering layer of neutral absorbing material with a low column density ($N_H \sim 1 \times 10^{22}\ \mathrm{cm^{-2}}$) is required by the data. This additional "full-covering low column" layer is only detectable when the central source is uncovered by the sometimes partial-covering high column absorber. Given its stability over at least ~2 months, it is likely not in the innermost regions of the nucleus. However, since the extended soft plasma emission is not attenuated by this absorber, it must be closer to the nucleus than the extended plasma. A third layer of partial covering "patchy" neutral absorption is distinguishable from the high column absorber by its unusual variability during observation 3. Note that while we only fit a single partial-covering absorber component, the drastic difference in

Table 2
Broadband Model Parameters

Interval	Unabsorbed Continuum $F_{2\text{-}10}$[a]	Photon Index (Γ)	PC Column Density ($N_{\rm H}$) (10^{22} cm^{-2})	Covering Fraction (f)	FC Column Density (10^{22} cm^{-2})	Scattered Power-Law $F_{0.5-2}$[a]/F_{2-10}[a]	Soft Gaussian at 0.68 keV Norm (10^{-5})	Relativistic Reflection Norm (10^{-6})	Distant Reflection Norm (10^{-6})	χ^2/dof
Obs. 1	16.8 ± 0.3	1.84 ± 0.02	22.4 ± 0.2	1.00[b] (>0.99)	1.0[c]	$0.27 / 0.38 \pm 0.01$	⋯	1.0 ± 0.0	3.0 ± 0.2	1627/1243
Obs. 2	27.3 ± 0.6	2.01 ± 0.01	8.4 ± 0.2	0.76 ± 0.01	1.4 ± 0.1	$0.44 / 0.52 \pm 0.03$	4.3 ± 1.3	2.0 ± 0.1	3.4 ± 0.4	2131/1353
Obs. 3	23.0 ± 0.5	2.04 ± 0.01	5.8 ± 0.4	0.49 ± 0.01	1.1 ± 0.1	$0.78 / 0.75 \pm 0.05$	20.5 ± 2.4	2.1 ± 0.1	3.2 ± 0.5	1877/1347
Obs. 4	21.6 ± 0.5	1.92 ± 0.01	11.3 ± 0.2	0.97 ± 0.01	1.0 ± 0.2	$0.35 / 0.46 \pm 0.02$	0.2[b] (<1.0)	1.5 ± 0.1	3.3 ± 0.3	1888/1323
P1	16.0 ± 0.7	1.87 ± 0.02	24.0 ± 0.5	1.00[b] (>0.99)	1.0[c]	$0.26 / 0.37 \pm 0.01$	⋯	1.1 ± 0.1	2.4 ± 0.4	953/804
P2	21.2 ± 1.1	1.90 ± 0.03	21.3 ± 0.5	1.00[b] (>0.99)	1.0[c]	$0.34 / 0.46 \pm 0.02$	⋯	1.3 ± 0.2	3.5 ± 0.6	918/708
P3	17.4 ± 1.2	1.89 ± 0.03	25.6 ± 0.8	1.00[b] (>0.99)	1.0[c]	$0.26 / 0.36 \pm 0.02$	⋯	1.2 ± 0.2	2.5 ± 0.6	641/544
P4	17.5 ± 1.3	1.91 ± 0.04	22.6 ± 0.7	1.00[b] (>0.99)	1.0[c]	$0.26 / 0.35 \pm 0.02$	⋯	1.2 ± 0.2	2.6 ± 0.7	569/515
P5	23.9 ± 1.2	2.05 ± 0.03	8.8 ± 0.4	0.82 ± 0.01	1.4[c]	$0.39 / 0.48 \pm 0.04$	1.5 ± 0.6	2.1 ± 0.2	4.7 ± 0.8	806/690
P6	31.2 ± 1.1	2.03 ± 0.02	8.2 ± 0.3	0.80 ± 0.01	1.4[c]	$0.36 / 0.51 \pm 0.03$	3.1 ± 0.5	2.6 ± 0.2	5.7 ± 0.8	1180/906
P7	23.1 ± 0.9	1.99 ± 0.02	7.8 ± 0.3	0.78 ± 0.01	1.4[c]	$0.39 / 0.54 \pm 0.03$	1.2 ± 0.5	1.9 ± 0.2	4.5 ± 0.7	1100/883
P8	27.5 ± 1.1	1.97 ± 0.02	7.8 ± 0.4	0.70 ± 0.01	1.4[c]	$0.45 / 0.62 \pm 0.04$	2.8 ± 0.6	1.7 ± 0.2	3.7 ± 0.8	1067/873
P9	16.4 ± 1.3	1.93 ± 0.04	9.1 ± 0.6	0.90 ± 0.01	1.1[c]	$0.49 / 0.69 \pm 0.08$	1.3 ± 1.7	1.8 ± 0.2	4.9 ± 1.0	529/536
P10	23.3 ± 1.1	2.00 ± 0.03	5.7 ± 0.4	0.75 ± 0.01	1.1[c]	$0.54 / 0.61 \pm 0.06$	10.7 ± 2.0	2.3 ± 0.3	3.8 ± 0.9	1102/774
P11	24.0 ± 1.1	2.04 ± 0.03	4.2 ± 0.4	0.59 ± 0.01	1.1[c]	$0.58 / 0.56 \pm 0.06$	15.1 ± 2.2	2.2 ± 0.2	6.6 ± 0.9	1102/768
P12	38.9 ± 1.3	2.07 ± 0.03	4.3 ± 0.6	0.29 ± 0.03	1.1[c]	$1.00 / 1.08 \pm 0.10$	31.5 ± 3.7	2.6 ± 0.3	4.3 ± 1.3	1011/874
P13	40.7 ± 1.3	2.07 ± 0.03	7.2 ± 0.2	1.00[b] (>0.99)	1.0[c]	$0.37 / 0.39 \pm 0.03$	0.2[b] (<1.0)	2.0 ± 0.3	2.5 ± 1.2	908/719
P14	18.9 ± 1.1	1.93 ± 0.04	11.7 ± 0.5	0.97 ± 0.01	1.0[c]	$0.33 / 0.43 \pm 0.05$	0.3[b] (<1.0)	1.6 ± 0.2	3.9 ± 0.9	556/592
P15	20.9 ± 0.8	1.90 ± 0.03	12.9 ± 0.3	0.98 ± 0.01	1.0[c]	$0.31 / 0.42 \pm 0.03$	2.0 ± 0.6	1.3 ± 0.1	3.4 ± 0.6	917/816
P16	20.8 ± 0.8	1.93 ± 0.02	16.9 ± 0.4	0.99 ± 0.01	1.0[c]	$0.34 / 0.44 \pm 0.03$	1.0 ± 0.6	1.4 ± 0.1	2.3 ± 0.5	1089/950

Notes. Best-fit parameters for the four observations and the 16 intervals, four per observation. PC and FC stand for partial-covering and full-covering, respectively. The intrinsic continuum fluxes and soft scattered power-law fluxes were determined using the PEGPWRLW model in XSPEC.

[a] Flux is in units of 10^{-12} erg cm^{-2} s^{-1}.

[b] Indicates a frozen parameter.

[c] Indicates a pegged parameter.

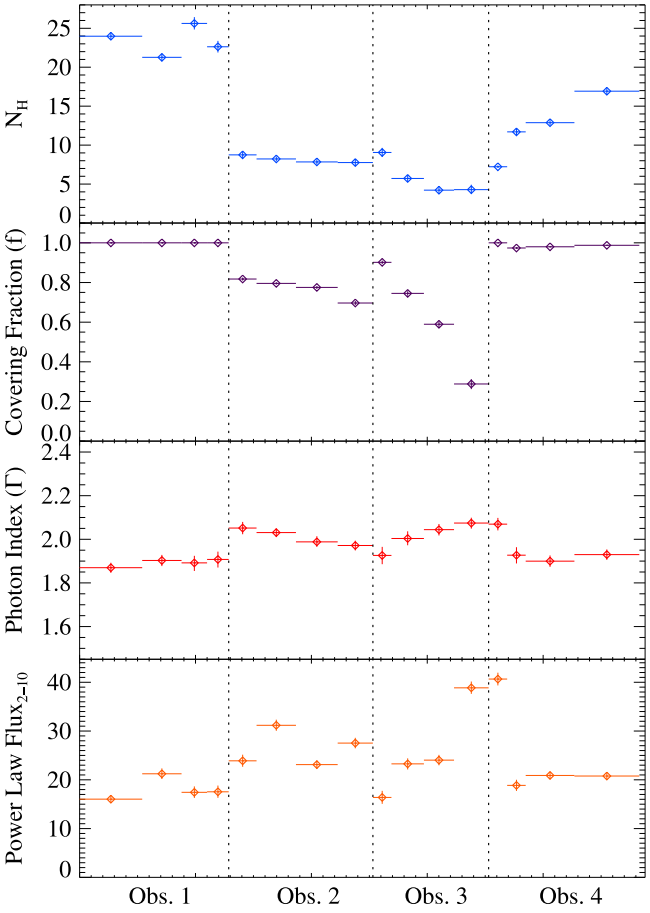

Figure 3. Parameter evolution from time-resolved fitting the 16 intervals (four per observation): column density, covering fraction, photon index, and the unabsorbed 2–10 keV flux.. The variation in column density is consistent with the hardness ratio evolution seen in Figure 1. The photon index is stable over each observation and does not vary greatly between observations while the intrinsic flux does vary greatly. N_H is in units of 10^{22} cm^{-2} and power-law flux is in units of 10^{-12} erg cm^{-2} s^{-1}.

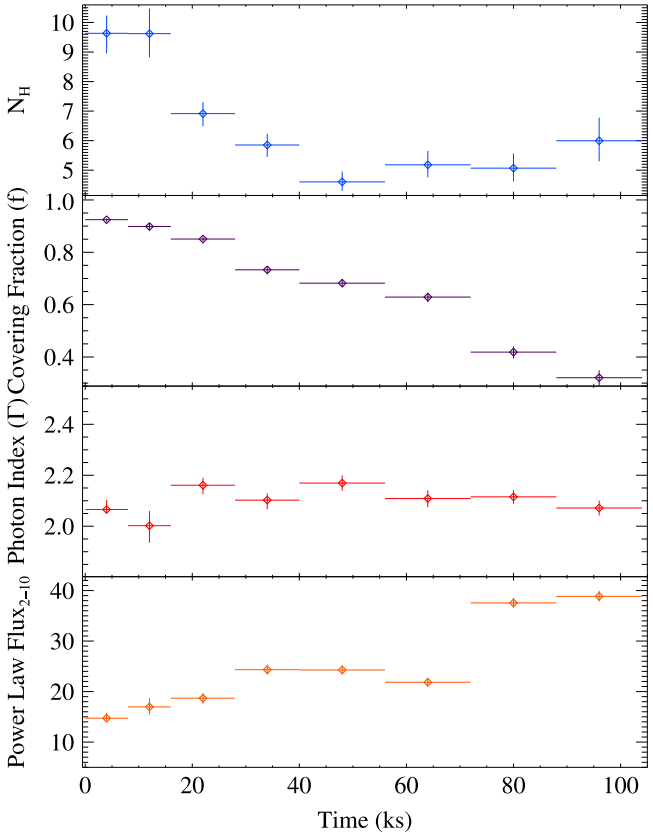

Figure 4. Parameter evolution over the course of observation 3: column density, covering fraction, photon index, and unabsorbed 2–10 keV flux. Note that the decreasing column density and covering fraction seem to have an inverse relationship with the increasing intrinsic flux, while the photon index is relatively stable. This unusual behavior for absorption variability may be indicative of a wind absorber scenario. N_H is in units of 10^{22} cm^{-2} and power-law flux is in units of 10^{-12} erg cm^{-2} s^{-1}.

behavior during the four different observations leads us to the conclusion that we are witnessing multiple layers of absorption dominating at different times.

4.1. The Nature of the Variable Absorber

The uncovering of the continuum by the high column partial covering absorber seen during 2012 December (observation 2) and 2013 January (observation 3) is an unusual event, particularly the extreme uncovering witnessed in the January observation, where both the column density and covering fraction dropped dramatically. This is in contrast to earlier observations of fast absorption variability due to "comet-like" BLR clouds, which show an increase in the covering fraction as the column density declines, indicative of a denser core leading a diffuse tail (Maiolino et al. 2010). The simultaneous drop in both the column density and the covering fraction in our third observation is inconsistent with this kind of event.

In order to discover the origin of the variability in the absorber we looked for relationships between the parameters that showed the greatest variations. Figure 10 shows the relationships between N_H and intrinsic flux, and between N_H and f. The flux plotted here is the unabsorbed power-law 2–10 keV flux which corresponds directly to the intrinsic

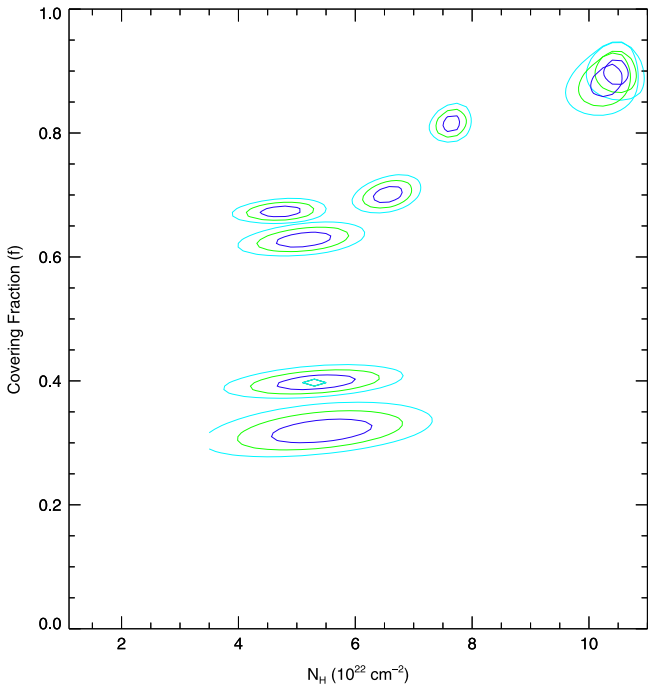

Figure 5. Observation 3 contour plots of N_H vs. f for the partial-covering "patchy" absorber in the eight subintervals, showing that there is very little degeneracy between these parameters. Levels are at 1σ, 2σ, and 3σ.

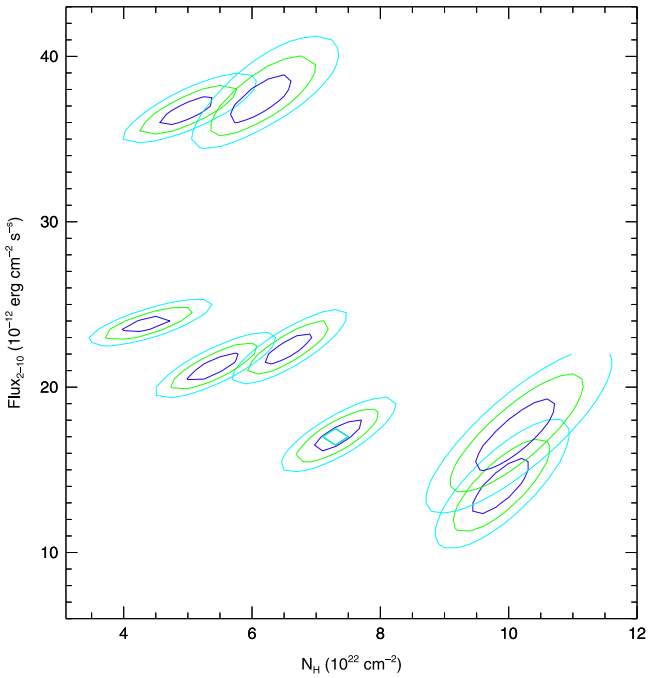

Figure 6. Observation 3 contour plots of intrinsic flux vs. N_H for the partial-covering "patchy" absorber in the eight subintervals. We see that there is some parameter degeneracy, but that it is not large and it is in the opposite sense to the observed evolution. Levels are at 1σ, 2σ, and 3σ.

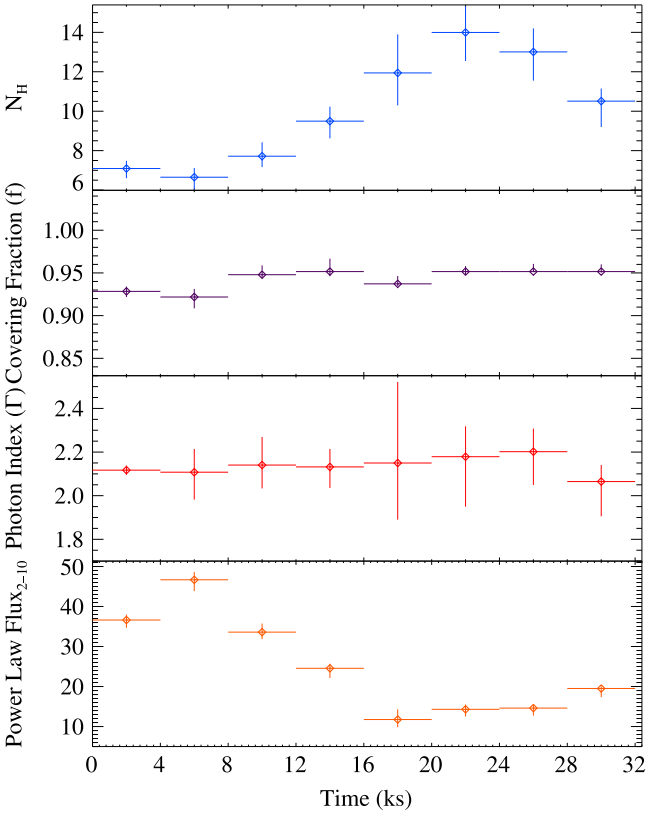

Figure 7. Parameter evolution for the first two intervals (32 ks) of observation 4 divided into eight equal time bins: column density, covering fraction, photon index, and unabsorbed 2–10 keV flux. Here the smooth increase and decrease in column density are reminiscent of occultation events seen in this source and others in the past, though there still seems to be an inverse relationship with the intrinsic flux. The covering fraction and photon index do not show significant evolution over this time period. N_H is in units of 10^{22} cm^{-2} and power-law flux is in units of 10^{-12} erg cm^{-2} s^{-1}.

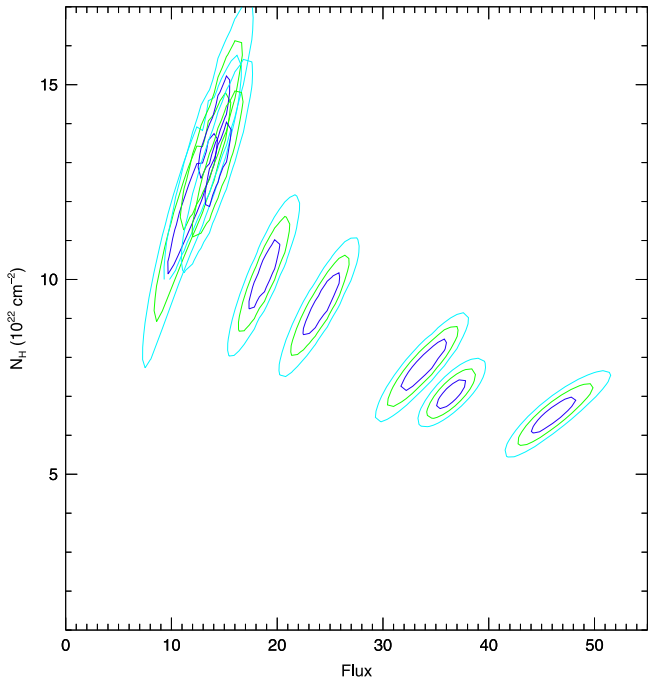

Figure 8. Observation 4 contour plots of intrinsic flux vs. N_H for the partial-covering absorber in the eight subintervals. We see that there is some parameter degeneracy, but that it is not large and it is in the opposite sense to the observed evolution. Levels are at 1σ, 2σ, and 3σ.

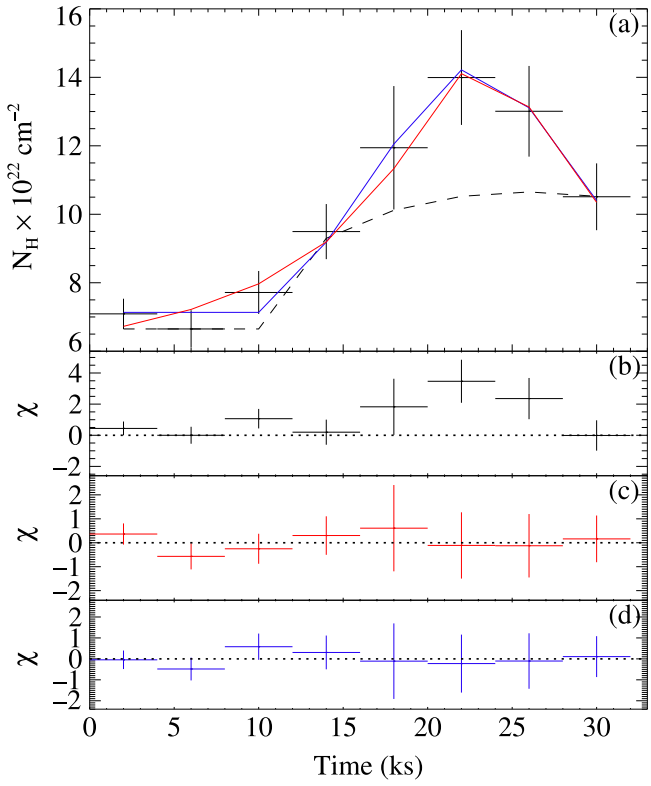

Figure 9. Fitting the occultation event in observation 4 with a solid sphere (dashed black), a beta profile ($\rho \propto r^{\beta}$; red), and a sphere of linear density profile ($\rho \propto r^{-1}$; blue). Residuals for the models are shown in (b), (c), and (d), respectively, showing that the latter two models both fit the data reasonably well.

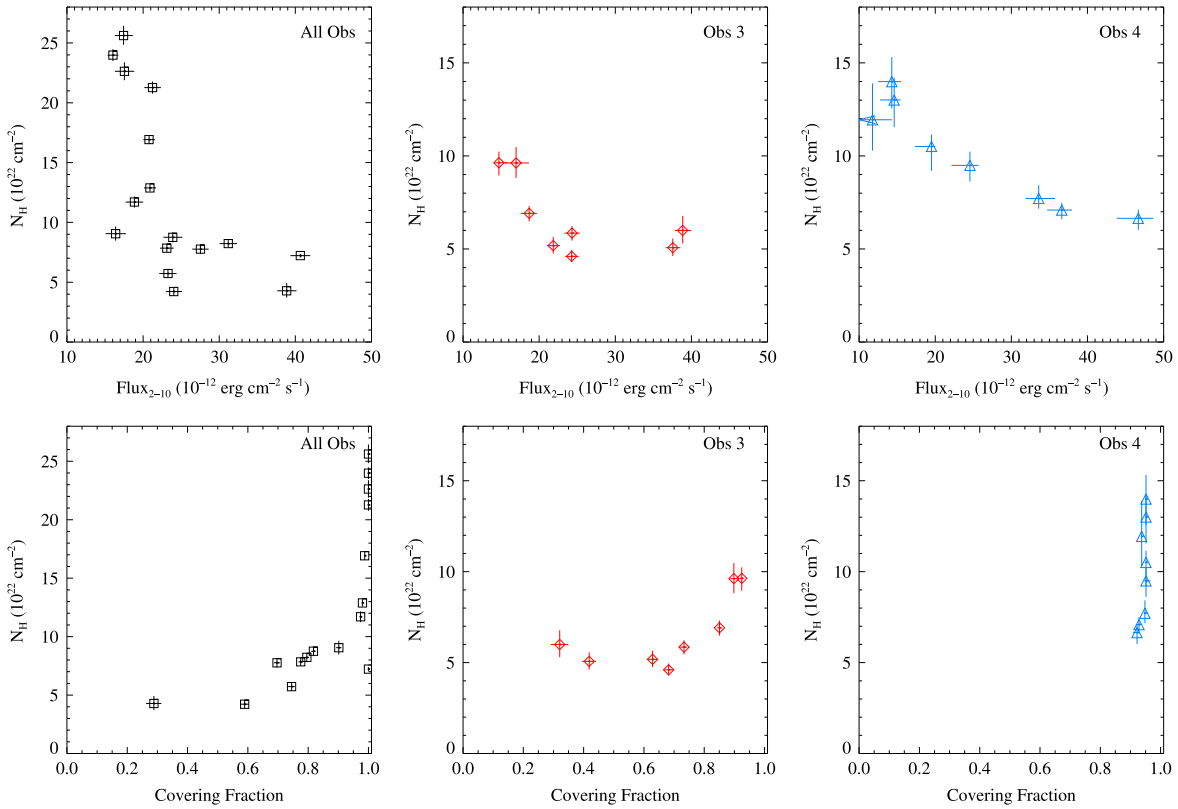

Figure 10. These plots show relationships between spectral fit parameters on the various analyzed intervals. Left: N_H vs. intrinsic power-law flux and N_H vs. covering fraction for the 16 time-resolved intervals (P1–16). Middle: N_H vs. intrinsic power-law flux and N_H vs. covering fraction for the eight half-intervals of observation 3. Right: N_H vs. intrinsic power-law flux and N_H vs. covering fraction for the 4 ks subintervals of the beginning of observation 4.

luminosity of the source. For the 16 intervals, N_H appears to be correlated with flux at the 99.5% level and with the covering fraction at the 99.9% level by the Pearson correlation test. These trends are also seen for the subintervals at around the ∼95% confidence level (although note the small sample sizes). There is some indication that on longer timescales the photon index softens as the source brightens (correlated at the 99.9% level for the 16 intervals). However, this correlation is not seen on shorter timescales (for the subintervals of observations 3 and 4).

The relationship between N_H and flux in observation 3 is consistent with the anti-correlation noticed by Connolly et al. (2014) from analyzing *Swift* monitoring data of NGC 1365. Our data do not show a simple linear correlation between these parameters. It seems clear, however, that when the X-ray source is brighter ($\gtrsim 2 \times 10^{-11}$ erg cm^{-2} s^{-1}) the column density is much lower ($\lesssim 1 \times 10^{23}$ cm^{-2}). For lower values of flux ($\lesssim 2 \times 10^{-11}$ erg cm^{-2} s^{-1}), the column density is much higher ($\gtrsim 1 \times 10^{23}$ cm^{-2}). Connolly et al. (2014) suggested that this could be due to a wind absorber which launches from further out when the source flux goes up.

This patchy wind absorber is only clearly seen in observation 3. In the other three observations a high column, sometimes partial-covering absorber dominates. This high column absorber is likely associated with the BLR (as evidence by the occultation event in observation 4 and those seen previously) as well as with the torus. The timescale of the uncovering between observations 2, 3, and 4 is weeks to months rather than hours, indicating that it is either due to a gap in the torus clouds or to a global attenuation of material. Since we do not see any other evidence of a temporary drop in overall accretion rate, we favor the former scenario.

One other possibility is that the drop in covering fraction in observation 3 could be explained by a cloud moving out of the line-of-sight. If the cloud were decreasing in size, such as with a drawn out filamentary tail, then instead of the comet-like increase in covering fraction we would see a shrinking covering fraction as less and less of the tail covered the source. This would match our observed absorption parameter evolution, though it does not explain the correlation between the absorber parameters and intrinsic flux seen in observation 3. We therefore reject this hypothesis.

4.2. Size of the X-ray Emitting Region

In this data set we see changes in the absorbers on multiple timescales. We see an initial drop in total column density over the course of ∼5 months from 22 to 8×10^{22} cm^{-2}. Then in observation 3 N_H goes from 11 to 4×10^{22} cm^{-2} in ∼130 ks while the covering fraction drops to 0.45. And in the first 20–24 ks of observation 4 N_H rises from 7 to 14×10^{22} cm^{-2}. This last value is the most rapid change and can be used to place constraints on the size of the X-ray emitting region. Since the occultation in observation 4 is nearly fully covering, we can infer that the X-ray emitting region is no larger than the size of the occulting cloud: $\lesssim 10\, R_g$.

This agrees with previous estimates of the compactness of the X-ray corona from the measured relativistic reflection, observed reverberation and BLR occultation events (Maiolino et al. 2010; Kara et al. 2015; Walton et al. 2014). However, it presents a conundrum when we consider the extremely low

covering fraction seen in observation 3. To see such a clear drop in covering fraction would require that the absorber be either very close to the source or made up of clumps/filaments that are smaller than the size of the X-ray emitting region. Since the drop in covering fraction occurs slowly over the entire observation and taking into account the low ionization state of the absorbers, the latter scenario seems more plausible, possibly due to a patchy disk wind.

4.3. Summary

Between 2012 July and 2013 February, *NuSTAR* and *XMM-Newton* performed four long-look joint observations of NGC 1365. We have analyzed the variable absorption seen in these observations in order to characterize the geometry of the absorbing material. Fortuitously, two of the observations caught the source in an unusually low absorption state, revealing additional complexity that had previously been hidden. This "peak between the clouds" allowed us to see past the typical torus/BLR clouds, which tend to have column densities of around $\sim 10^{23}$ cm^{-2}, uncovering a patchy absorber with a variable column around $\sim 10^{22}$ cm^{-2} and a measured covering fraction of $f = 0.3$–0.9. Additionally, we found that this patchy absorber seems to respond to the intrinsic source flux, with the column density and covering fraction dropping as the source grows brighter. This could be due to a high luminosity event pushing an absorbing wind out to a large radius where the covering fraction and effective $N_{\rm H}$ both drop dramatically. This latter theory is espoused by Connolly et al. (2014), who noticed an anti-correlation between $N_{\rm H}$ and luminosity in NGC 1365, a trend which our data confirms.

We also find evidence of an additional constant absorber with a low column density of 1×10^{22} cm^{-2}, the geometrical location of which is still unclear. The ionized wind absorbers seen in this source (Risaliti et al. 2005; Braito et al. 2014) most likely reside closer to the central source than the three layers of neutral absorbers we have characterized in this work.

A short occultation event in 2013 February was observed, likely due to a BLR clump passing through the line-of-sight. We estimate a clump size of $\sim 4 \times 10^{12}$ cm with a central density of $\sim 3 \times 10^{10}$ cm^{-3}. From this we also infer a small X-ray corona with a linear dimension of only a few $R_{\rm g}$.

This work was supported under NASA Contract No. NNG08FD60C, and made use of data from the *NuSTAR* mission, a project led by the California Institute of Technology, managed by the Jet Propulsion Laboratory, and funded by the National Aeronautics and Space Administration. We thank the *NuSTAR* Operations, Software, and Calibration teams for support with the execution and analysis of these observations. This research has made use of the *NuSTAR* Data Analysis Software (NuSTARDAS) jointly developed by the ASI Science Data Center (ASDC, Italy) and the California Institute of Technology (USA). This work has also made use of HEASARC online services, supported by NASA/GSFC, and the NASA/IPAC Extragalactic Database, operated by JPL/California Institute of Technology under contract with NASA. This work also made use of data from the *XMM-Newton* observatory.

Facilities: NuSTAR, *XMM*

REFERENCES

Anders, E., & Grevesse, N. 1989, GeCoA, 53, 197
Arnaud, K. A. 1996, in ASP Conf. Ser. 101, Astronomical Data Analysis Software and Systems V, ed. G. Jacoby, & J. Barnes (San Francisco, CA: ASP), 17
Braito, V., Reeves, J. N., Gofford, J., Nardini, E., Porquet, D., & Risaliti, G. 2014, ApJ, 795, 87
Brenneman, L. W., Risaliti, G., Elvis, M., & Nardini, E. 2013, MNRAS, 429, 2662
Connolly, S. D., McHardy, I. M., & Dwelly, T. 2014, MNRAS, 440, 3503
Eguechi, S., Ueda, Y., Terashima, Y., Mushotzky, R., & Tueller, J. 2009, ApJ, 696, 1657
García, J., & Kallman, T. R. 2010, ApJ, 718, 695
George, I. M., & Fabian, A. C. 1991, MNRAS, 249, 352
Guainazzi, M., Matt, G., & Perola, G. C. 2005, A&A, 444, 119
Guainazzi, M., Risaliti, G., Nucita, A., et al. 2009, A&A, 505, 589
Harrison, F. A., Craig, W. W., Christensen, F. E., et al. 2013, ApJ, 770, 103
Kara, E., Zoghbi, A., Marinucci, A., et al. 2015, MNRAS, 446, 737
Kalberla, P. M. W., Burton, W. B., Hartmann, D., et al. 2005, A&A, 440, 775
Lamer, G., Uttley, P., & McHardy, I. M. 2003, MNRAS, 342, L41
Maiolino, Risaliti, G., Salvati, M., et al. 2010, A&A, 517A, 47
Marinucci, A., Matt, G., Miniutti, G., et al. 2014, ApJ, 787, 83
Nenkova, M., Sirocky, M. M., Nikutta, R., Ivezić, Ž., et al. 2008, ApJ, 685, 160
Parker, M. L., Walton, D. J., Fabian, A. C., & Risaliti, G. 2014, MNRAS, 441, 1817
Risaliti, G., Bianchi, S., Matt, G., et al. 2005, MNRAS, 630, 129
Risaliti, G., Harrison, F. A., Madsen, K. K., et al. 2013, Natur, 494, 449
Risaliti, G., Miniutti, G., Elvis, M., et al. 2009, ApJ, 696, 160
Rivers, E., Markowitz, A., & Rothschild, R. 2011, ApJ, 742, 29
Rivers, E., Markowitz, A., Rothschild, R., et al. 2014, ApJ, 786, 126
Strüder, L., Briel, U., Dennerl, K., et al. 2001, A&A, 365, L18
Turner, T. J., George, I. M., Nandra, K., & Mushotzky, R. F. 1997, ApJS, 113, 23
Turner, T. J., Reeves, J. N., Kraemer, S. B., & Miller, L. 2008, A&A, 483, 161
Turner, M. J. L., Abbey, A., Arnaud, M., et al. 2001, A&A, 365, 27
Verner, D. A., Ferland, G. J., Korista, K. T., & Yakovlev, D. G. 1996, ApJS, 465, 487
Walton, D., Reis, R. C., & Fabian, A. C. 2010, MNRAS, 408, 601
Walton, D., Risaliti, G., Harrison, F. A., et al. 2014, ApJ, 788, 76
Wang, J., Fabbiano, G., Elvis, M., et al. 2009, ApJ, 694, 718